OPEN ACCESS

ARTICLE

The Innovation Materials

Molecular engineering on hole injection self-assembled monolayers for superior RGB quantum dot light-emitting diodes

Wanhai Wang,[1,2,4] Qiyin Chen,[2,4] Guoxin Hua,[2] Jie Lin,[3] Jingsong Huang,[3] Guohua Xie,[2,*] and Weihua Tang[1,2,*]

*Correspondence: ifeghxie@xmu.edu.cn (G.X.); whtang@xmu.edu.cn (W.T.)

Received: February 27, 2025; Accepted: June 26, 2025; Published Online: July 7, 2025; https://doi.org/10.59717/j.xinn-mater.2025.100151

GRAPHICAL ABSTRACT

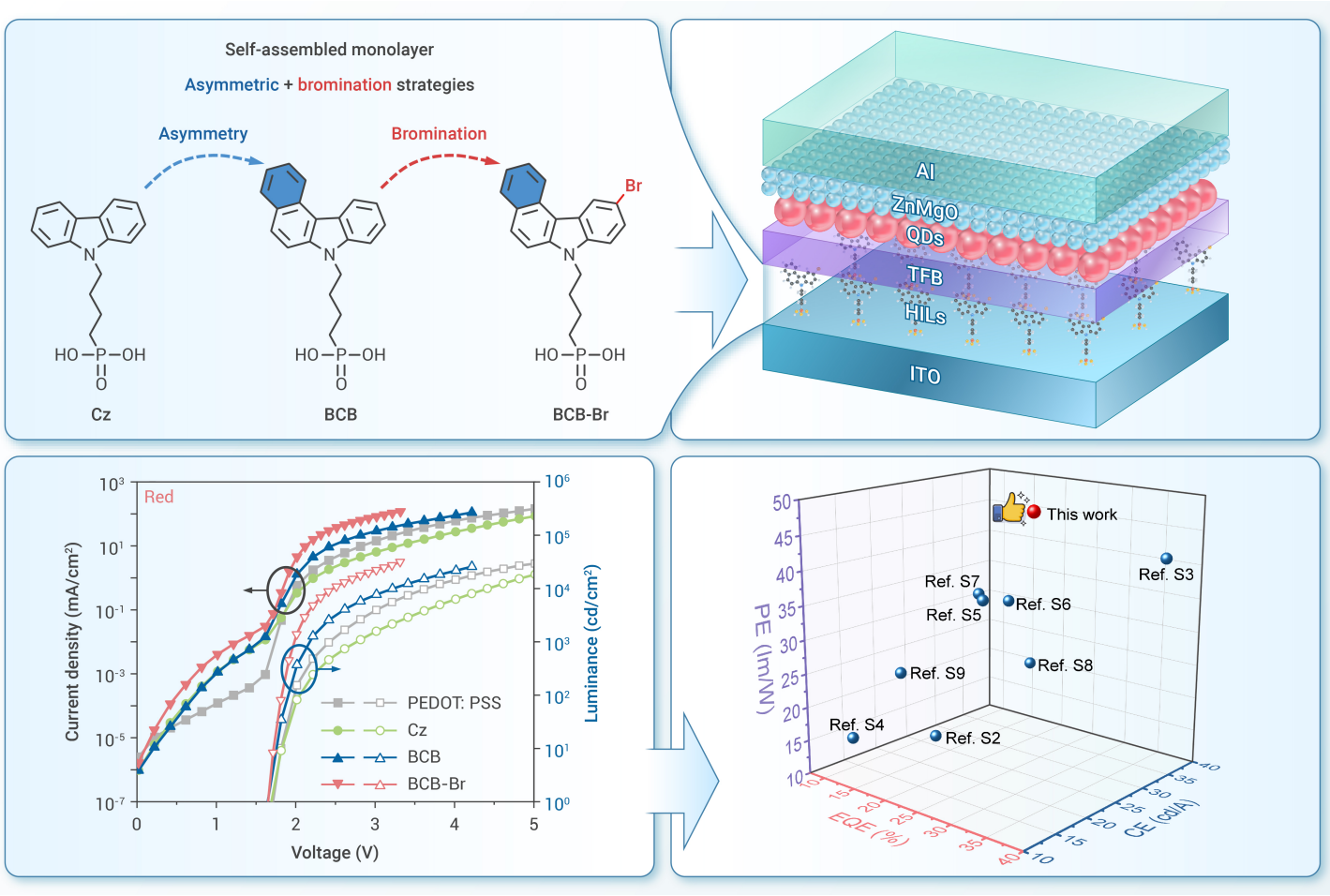

PUBLIC SUMMARY

- SAMs are promising alternatives to problematic PEDOT:PSS for efficient QLEDs.
- Comprehensive molecular engineering enhanced the SAMs' interface modification capability.
- The BCB-Br based red QLEDs deliver one of the highest EQE, PE and CE values with a low V_t.
- BCB-Br demonstrates excellent compatibility in green and blue QLEDs.

ARTICLE

OPEN ACCESS

www.the-innovation.org/materials

Molecular engineering on hole injection self-assembled monolayers for superior RGB quantum dot light-emitting diodes

Wanhai Wang,[1,2,4] Qiyin Chen,[2,4] Guoxin Hua,[2] Jie Lin,[3] Jingsong Huang,[3] Guohua Xie,[2,*] and Weihua Tang[1,2,*]

[1]College of Materials, College of Chemistry and Chemical Engineering, Innovation Laboratory for Sciences and Technologies of Energy Materials of Fujian Province (IKKEM), Xiamen University, Xiamen 361005, China

[2]Institute of Flexible Electronics (IFE, Future Technologies), Xiamen University, Xiamen 361005, China

[3]Oxford Suzhou Centre for Advanced Research (OSCAR), University of Oxford, Suzhou 215123, China

[4]These authors contributed equally

*Correspondence: ifeghxie@xmu.edu.cn (G.X.); whtang@xmu.edu.cn (W.T.)

Received: February 27, 2025; Accepted: June 26, 2025; Published Online: July 7, 2025; https://doi.org/10.59717/j.xinn-mater.2025.100151

Citation: Wang W., Chen Q., Hua G., et al. (2025). Molecular engineering on hole injection self-assembled monolayers for superior RGB quantum dot light-emitting diodes. *The Innovation Materials* **3**:100151.

Colloidal quantum dot light-emitting diodes (QLEDs) show strong performance dependence on efficient hole injection and balanced carrier injection. The widely used hole-injection layer (HIL) poly(3,4-ethylenedioxythiophene): poly(styrenesulfonate) (PEDOT:PSS) suffers from inherent strong acidity, high cost and mismatched work function (WF) with transparent anodes in QLEDs. In this study, we propose herein molecular engineering on self-assembled monolayers (SAMs) as promising HILs to fabricate efficient red, green and blue QLEDs. Asymmetric conjugation extension and bromination on carbazole core strategically modulate the SAMs in dipole moment and interfacial modification of ITO's WF. The 4-(10-bromo-7*H*-benzo[*c*]carbazol-7-yl)butyl)phosphonic acid (BCB-Br) constructs the optimal cascade energy level alignment for hole injection. SAMs based HILs with exceptional uniformity and conductivity afford significantly enhanced hole injection and reduced interfacial contact resistance in QLEDs. The BCB-Br HIL based red QLEDs contribute an impressive external quantum efficiency of 23.3% and a notably low turn-on voltage of 1.73 V. Moreover, the devices are endowed with commendable power efficiency of 47.0 lm/W and current efficiency of 30.4 cd/A, among the highest values across the critical QLEDs performance metrics in the literature. The university of SAMs as excellent HILs is further demonstrated by the superior electroluminescence (EL) performances in both green and blue QLEDs over PEDOT:PSS. These findings underscore the efficacy of molecular designed SAMs to boost the interface modification on transparent anodes, offering valuable insights for the development of new HILs for QLEDs.

INTRODUCTION

Colloidal quantum dot light-emitting diodes (QLEDs) have emerged as a promising next-generation technology for displays and lighting, owing to their superior color purity, brightness, energy efficiency, and cost-effective device fabrication.[1-3] Structurally, conventional QLEDs feature a multilayer architecture of transparent anode/hole-injection layer (HIL)/hole-transporting layer (HTL)/quantum dot emissive layer (EML)/electron-transporting layer (ETL)/metal cathode, where the HIL plays a crucial role in hole injection and transport from the anode into the HTL, significantly influencing the overall device performance.[4] Great research efforts have thus been concentrated in developing highly efficient and stable QLEDs via simple and fully solution manufacturing techniques.

Traditionally, poly(3,4-ethylenedioxythiophene):poly(styrenesulfonate) (PEDOT:PSS) serves as the preferred HIL material due to its high transparency, excellent conductivity, and favorable film-forming properties.[5-7] However, its widespread adoption has been restricted by inherent acidity, elevated costs, and limited capacity to effectively modify the work function (WF) of transparent conductive oxide (TCO, like ITO: indium tin oxide) electrodes.[8,9] The modifications on PEDOT:PSS or replacement of it with metal oxides (such as NiO_x, MoO_x, and CuO_x) HILs can mitigate some of these issues though,[10-12] these alternative solutions often necessitate complex and high-temperature processing to further escalate the fabrication costs and energy consumption. Considering these challenges, the development of cost-effective high-efficient HILs is essential for promoting the practical application of QLEDs.

Among the range of candidates, self-assembled monolayers (SAMs) featuring conjugated terminal for charge extraction and anchoring groups for surface modification on TCO electrodes possess significant potential for high-throughput solution manufacturing of high-performance organic/perovskite solar cells, field effect transistors, and perovskite light-emitting diodes (PeLEDs).[13-15] Such materials can spontaneously self-assemble into well-spreading compact films from solutions on TCO substrates for better interface contact and energy level alignment, facilitating hole extraction/transport from adjacent functional layers to make the state-of-the-art new generation optoelectronics.[16-18] Besides, the ultrathin SAMs films ensure high light transmittance and efficient charge transfer via tunneling effect. The improved interface contact and optimized charge injection therefore lead to significantly enhanced electroluminescent (EL) performance in PeLEDs.[14] In addition, different from metal oxides typically prepared from energy-intensive processes and susceptible to vacancy defects,[19] SAMs can be developed with facile synthesis, adjustable energy levels, and scalability.[20,21] Nevertheless, the applications of SAMs in QLEDs remains underexplored. Challenges needed to be tackled include protracted self-assembly time of SAMs (up to 10 h), suboptimal device performance,[22,23] and correlation between SAMs molecular structure and QLEDs performance. In-depth research in this domain is thus imperative for advancing solution-processed QLED technology.

In this study, we have herein developed a novel class of SAMs featuring conjugation extended terminal and phosphonic acid anchoring groups as HILs for efficient QLEDs. These SAMs demonstrate remarkable self-assembly capacity and fast surface spreading over ITO surface within seconds. Molecular engineering on carbazole core synergistically enhanced the SAMs' solution-processability, dipole moment and the highest occupied molecular orbital (HOMO) energy levels. The optimal SAMs, i.e., 4-(10-bromo-7*H*-benzo[*c*]carbazol-7-yl)butyl)phosphonic acid (BCB-Br), contributes the deepest intrinsic HOMO level and the highest dipole moment, enabling effective modification on ITO's WF for improved energy level alignment. Importantly, the spin-coated BCB-Br films afford superior uniform, compact and conductive HILs for balanced hole injection and carrier recombination. The BCB-Br HIL based red QLEDs deliver a reduced turn-on voltage (V_t) (1.73 V) and a high external quantum efficiency (EQE) (23.3%), substantially surpassing those based on PEDOT:PSS (1.81 V, 21.6%) or unoptimized SAM (1.83 V, 19.4%) counterparts. Importantly, the commendable power efficiency (PE) of 47.0 lm/W and current efficiency (CE) of 30.4 cd/A establish them among the highest-performing devices that excel across these critical performance metrics in the literature. Notably, BCB-Br HILs demonstrate excellent compatibility in green (EQE=17.3%) and blue (EQE=8.7%) QLEDs, underscoring its versatility across the entire RGB spectrum. This research offers valuable insights for optimizing SAMs-based HILs and highlights their potential to enhance QLED performance.

MATERIALS AND METHODS

Materials

BCB-Br together with other two SAMs (ca. Cz and BCB) were synthesized in our laboratory (Scheme S1). Chlorobenzene and dimethyl sulfoxide were procured from Sigma-Aldrich Ltd. Ethanol, isopropanol, acetone and octane were acquired from Shanghai Titan Scientific Co., Ltd. Poly(ethylene-

dioxythiophene):polystyrenesulfonate (PEDOT:PSS, AI 4083) was obtained from Heraeus, Inc. Poly(9,9-dioctylfluorene-alt-*N*-(4-sec-butylphenyl)-diphenylamine) (TFB) was purchased from Luminescence Technology Corp. The red/green/blue (R/G/B) quantum dots and ZnMgO solutions were supplied from Mesolight Inc. All chemicals were used as received.

Fabrication of QLEDs

The patterned ITO substrates were subjected to ultrasonic cleaning in ethanol, acetone, and isopropanol solutions, with each treatment lasting 15 min. The substrates were then dried in an oven at 80°C. Before proceeding with device fabrication, ITO substrates underwent plasma treatment for 7 min to enhance surface properties. For the hole injection layers, PEDOT:PSS (AI 4083) solutions filtered through 0.22 μm polyvinylidene fluoride (PVDF) filters were spin-coated onto ITO substrates at 3000 rpm for 40 s, followed by thermal annealing at 150°C for 30 min in air. For preparing SAMs films, BCB-Br (or Cz, BCB) solutions in dimethyl sulfoxide (0.5 mg/mL) were drop-cast onto ITO substrates and allowed to stand for 30 s to facilitate effective assembly within nitrogen-filled glove box (O_2 < 1 ppm, H_2O < 1 ppm) before spin-coating. Subsequently, the substrates were spin-coated at 4000 rpm for 40 s before annealed at 120°C for 10 min. Once the HILs were established, layers of TFB (chlorobenzene, 8 mg/mL), CdZnSe/ZnS quantum dots (octane, 17 mg/mL), and ZnMgO (ethanol, 25 mg/mL) were sequentially spin-coated at 3000 rpm. Each layer underwent annealing at specific temperatures: 130°C for 30 min, 100°C for 10 min, and 80°C for 10 min. The samples were then transferred to a high-vacuum deposition chamber at a pressure of approximately 5×10^{-4} Pa for the deposition of a 100 nm thick aluminum top cathode. The effective area of the device was set at 4 mm^2. After the fabrication process was completed, the devices were encapsulated using UV-curable adhesive within the glove box to ensure stability and functionality.

Characterization

The energy-dispersive X-ray spectroscopy (EDS) images were observed using a field emission scanning electron microscope (Zeiss, Gemini SEM 500). Theoretical calculations concerning molecular geometry, energy levels, electrostatic surface potentials (ESP), and dipole moment were performed based on density functional theory (DFT) utilizing the B3LYP/6-31G (d, p) basis set. Molecular surface electrostatic potentials were mapped using Visual Molecular Dynamics (VMD), with the Van der Waals surface defined at 0.001 e $Bohr^{-3}$. The work functions of different HILs were determined through ultraviolet photoelectron spectroscopy (UPS) utilizing a Thermo Fisher ESCALAB Xi^+ instrument. Conductive atomic force microscopy (C-AFM) measurements were conducted on a Cypher ES (Oxford Instruments Asylum Research) in alternating current (AC) mode at 2.44 Hz using an ASYELEC.01-R2 probe. Absorption and transmittance spectra were recorded with a UV-3600 spectrophotometer (SHIMADZU). Water contact angles for PEDOT:PSS and SAM films were measured with a DSA25E instrument (Kruss). The current density-voltage-luminance (*J-V-L*) characteristics and electroluminescence (EL) spectra were captured using the M3000 measurement system (McScience). Additionally, transient electroluminescence (TREL), electrochemical impedance spectroscopy (EIS), and capacitance-voltage (*C-V*) characteristics were assessed with the all-in-one measurement system Paios 4.3 (Fluxim).

RESULTS AND DISCUSSION

Molecular design and material properties

SAMs are typically comprised of an anchoring group, a spacer linkage, and a conjugated terminal. The anchoring groups bond with TCO electrodes to promote interface interactions and surface wetting for solution spreading.[24] Molecular design on SAMs should thus take a good consideration on modulating the film-forming dynamic, molecule density and tolerance to subsequent layer deposition. We herein select phosphonic acid as the anchoring group owing to its superior binding strength and weaker acidity in comparison to sulfonic and carboxylic acids.[25] For the spacer, which bridges the anchoring and terminal groups, a medium-length butyl (C4) chain was employed. Compared to ethyl (C2) and hexyl (C6) chains, this spacer not only improves the solubility of the molecule but also ensures efficient charge injection capabilities.[26] Furthermore, the butyl spacer imparts enhanced molecular flexibility to SAMs, better accommodating mechanical stresses that may arise during device operation. The conjugation terminal incorporated into SAMs dictates the energy levels, dipole moment, intermolecular π-π interactions and film-forming properties of the monolayers.[27] Initially, we employed carbazole as the conjugation terminal in light of its appropriate HOMO energy level, easy-to-modify structure and commercial availability.[28] However, the highly coplanar structure of carbazole led to excessive molecular aggregation, which manifests as relatively poor solubility and suboptimal film-forming properties.[29] Additionally, the structural symmetry of carbazole also limits charge delocalization, thereby hindering the generation of a high intrinsic dipole moment–an essential factor for effectively modifying the ITO WF. To overcome these challenges, we introduced an asymmetric terminal group, specifically benzo[*c*]carbazole, to enhance both the solubility and the dipole moment of the resulting SAMs.[30] Upon incorporating an electron-withdrawing bromine (Br) atom into the asymmetric benzo[*c*]carbazole unit,[31] these improvements are further amplified. Such molecular engineering synergistically optimizes the intrinsic electrochemical properties and interface-modifying capabilities of the SAMs, which are expected to facilitate the hole injection process at the interface.

The as-designed SAMs were synthesized according to our previous reports,[31] with their molecular structures depicted in Figure 1A. The utilization of inexpensive raw materials coupled with straightforward purification offers a notable economic advantage for our SAMs with an estimated production cost of approximately $20 per gram in the lab (Table S1), which is attractive to replace the conventional PEDOT:PSS (~3000 $/L). A schematic depiction of QLEDs configuration utilizing these SAMs as HILs is illustrated in Figure 1B. To vividly elucidate the geometric and electronic structures of the SAMs, we performed density functional theory (DFT) calculations at the B3LYP/6–31G(d,p) level. The HOMO energy levels of the three SAMs, predominantly residing on the carbazole skeleton, were calculated as −5.37 eV for [4-(9*H*-carbazol-9-yl)butyl]phosphonic acid (Cz), −5.25 eV for (4-(7*H* benzo[*c*]carbazol-7-yl)butyl)phosphonic acid (BCB), and −5.46 eV for BCB-Br (Figure S1). The electrostatic surface potential (ESP) analysis was further conducted to visualize the charge distribution across the molecules (Figure 1C). The ESP mappings unveil the predominant concentration of negative electrostatic potential (in red color) at the conjugation terminal, while the positive electrostatic potential (in blue color) is primarily localized at spacer and anchoring groups. This charge polarization facilitates the generation of a high intrinsic dipole moment.[32] Specifically, compared to the symmetric Cz (μ=1.93 D), the asymmetric BCB achieves an increased dipole moment (2.28 D). The further introduction of Br into BCB endows BCB-Br with significantly enhanced dipole moment to 4.04 D. Notably, SAMs with large molecular dipoles and low-lying HOMO energy levels are advantageous for eliciting a downshift in the WF of ITO.

Subsequently, we conducted ultra-violet photoelectron spectroscopy (UPS) measurements to evaluate the impact of SAMs on the WF of ITO. The WF can be calculated using the equation WF = $h\nu - E_{cut\text{-}off}$, where $h\nu$ is 21.22 eV and $E_{cut\text{-}off}$ denotes the energy of the secondary electron cut-off, as illustrated in Figure 1D. The WF of PEDOT:PSS-modified ITO was determined to be 4.98 eV, which aligns with the reported value in the literature.[33] After surface deposition of Cz and BCB, the WF of ITO was modified to be 4.95 eV and 5.00 eV, respectively. Surprisingly, a much elevated WF (5.26 eV) was further achieved for ITO with BCB-Br modification. Such drmatically enhanced WF facilitates superior energy level alignment with the HTL (Figure S2), effectively minimizing recombination energy losses associated with hole injection at the HIL/HTL interface.

SAMs with phosphonic acid anchoring groups are known to spontaneously form atomically thin layers on TCO electrodes.[34] To validate the self-assembly characteristics of these SAMs, X-ray photoelectron spectroscopy (XPS) was utilized to analyze the elemental composition of the SAM-modified ITO. As illustrated in Figure 1E, a notable shift of the In 3d peaks to higher binding energies is observed for all SAM-modified ITO substrates in comparison to the pristine, confirming the robust interaction between SAMs and ITO surface. Afterwards, ultraviolet-visible (UV-vis) transmittance spectroscopy was employed to evaluate the optical properties variation with the deposition of SAMs films on ITO surface (Figure 1F). Notably, all SAM-modified ITO substrates exhibited high transmittance across the entire visible spectrum,

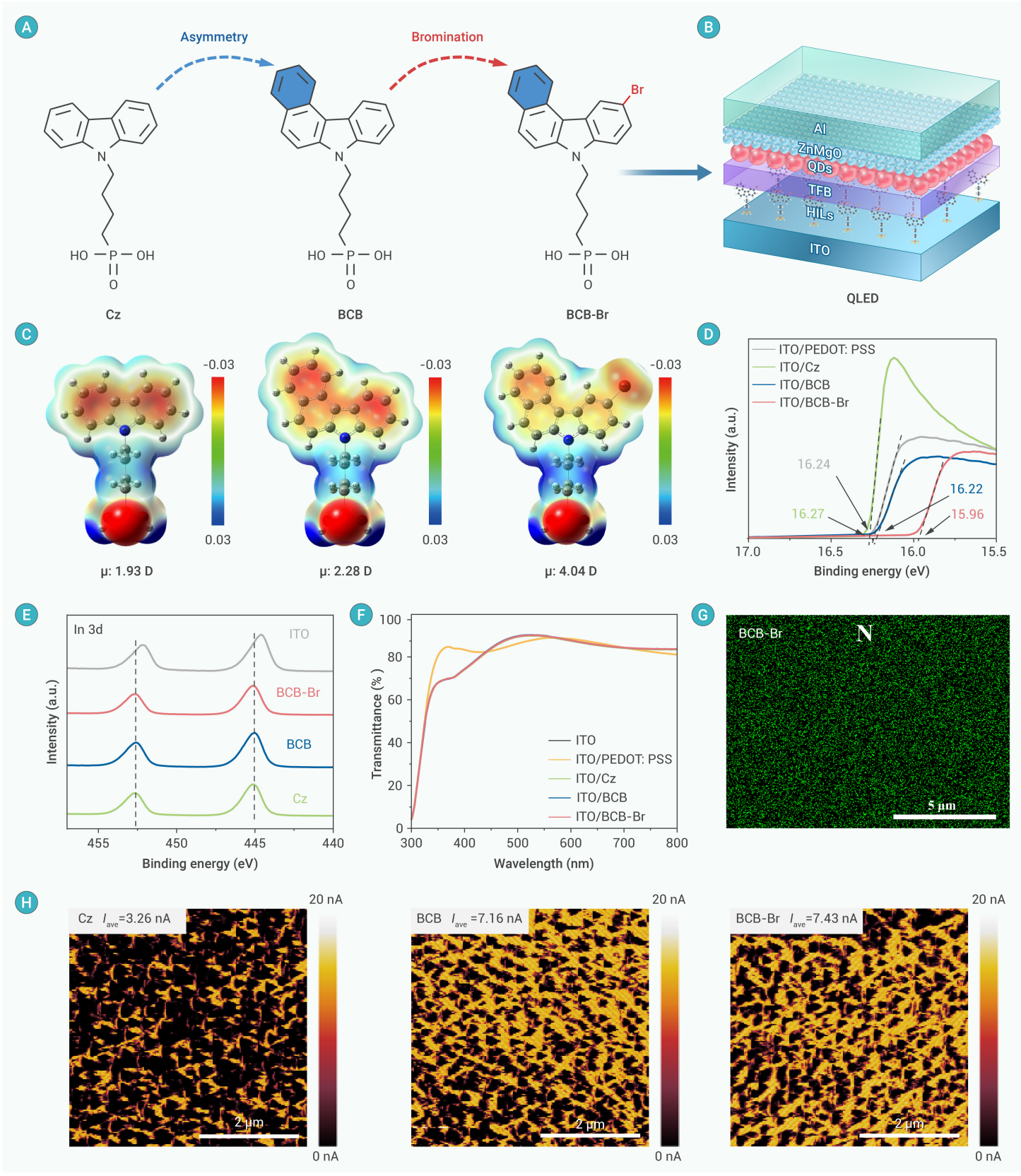

Figure 1. Molecular structures of SAMs and characterizations of their films (A) Molecular engineering on SAMs. (B) Schematic diagram of stacked QLED device structure. (C) ESP analysis of three SAM molecules. (D) UPS measurements of modified ITO substrates, (E) XPS and (F) UV-vis transmittance spectra of SAMs and PEDOT:PSS films modified ITO substrates. (G) Elemental mapping of N (green) for BCB-Br film spin-coated on ITO obtained using EDS. (H) C-AFM images of three SAM films spin-coated on ITO and the corresponding average currents.

closely resembling that of the bare ITO. In contrast, the PEDOT:PSS coated ITO displayed higher transmittance in the short wavelength range of 300–450 nm, while a relatively reduced transmittance in the 450–550 nm range.

The film coverage and homogeneity of SAMs on ITO substrates after rinsing with dimethyl sulfoxide (DMSO) were further investigated using energy-

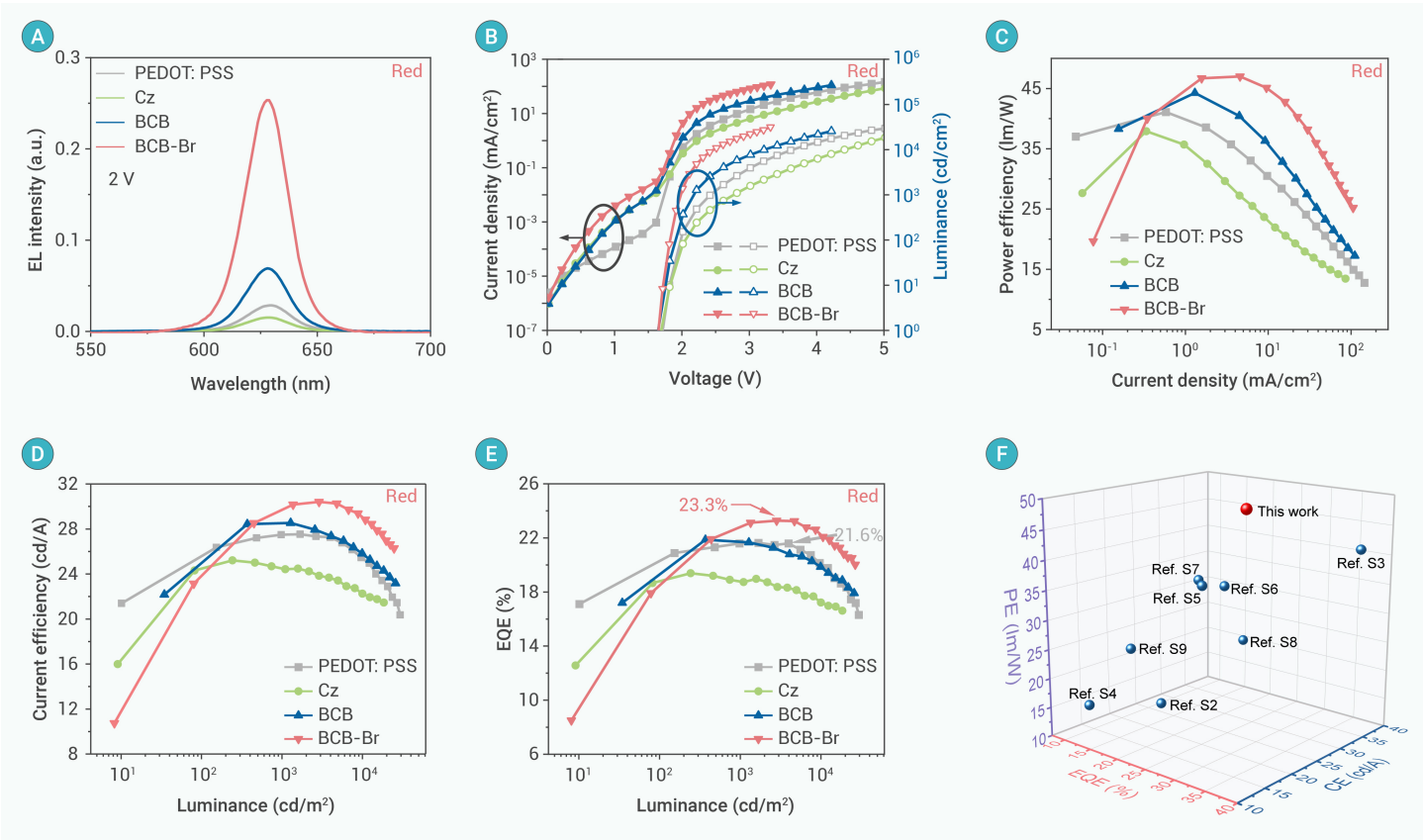

Figure 2. The EL performances of the red QLEDs utilizing SAMs or PEDOT:PSS as the HILs (A) EL spectra at 2 V, (B) the current-voltage-luminance (*J-V-L*), (C) power efficiency (PE), (D) current efficiency (CE) and (E) EQE curves of SAMs or PEDOT:PSS-based red QLEDs. (F) The EL performance comparison for CdZnSe/ZnS red QLEDs in this work with the literature reports (see Ref. S1-S9 in Table S2).

Table 1. EL performance parameters of SAMs or PEDOT:PSS-based red QLEDs

HILs	V_t[a] (V)	λ_{EL}[b] (nm)	FWHM[c] (nm)	PE[d] (lm/W)	CE[e] (cd/A)	EQE[f] (%)	CIE[g] (x, y)
PEDOT:PSS	1.81	628	22.7	41.1	27.5	21.6	(0.68, 0.31)
Cz	1.83	628	22.6	37.9	25.2	19.4	(0.68, 0.31)
BCB	1.75	628	22.2	44.3	28.5	21.9	(0.68, 0.31)
BCB-Br	1.73	628	22.4	47.0	30.4	23.3	(0.68, 0.31)

[a] Turn-on voltage at a luminance of 1 cd/m^2. [b] Peak wavelength of the EL spectrum. [c] Full-width at half-maximum of the EL spectrum. [d] Maximum power efficiency. [e] Maximum current efficiency. [f] Maximum external quantum efficiency. [g] Commission International de l'Éclairage 1931 color coordinates.

dispersive X-ray spectroscopy (EDS) analyses, where nitrogen (N) was selected as the characteristic element for molecular identification. As illustrated in Figure 1G, the nitrogen mapping of BCB-Br film demonstrates a highly homogeneous distribution without noticeable segregation. Comparative analysis for P and C atoms also shows no discernible differences, similar to those in Cz and BCB samples (Figure S3). For a more in-depth exploration of the film characteristics, conductive atomic force microscopy (C-AFM) measurements were undertaken. As illustrated in Figure 1H, the BCB-Br film exhibits an average current of 7.43 nA, slightly higher than that of BCB film (7.16 nA). In contrast, the Cz film displays a dramatically lower average current (3.16 nA), accompanied by inferior uniformity. The AFM height images further elucidate that the BCB-Br film possesses a smoother morphology with an average root mean roughness (RMS) of 2.85 nm, compared to 3.19 and 2.98 nm for Cz and BCB counterparts (Figure S4), respectively. These results highlight our molecular engineering synergistically enhances the film-forming quality and interface modification of SAMs. Concurrently, the hydrophobicity of the various SAM films was investigated via water contact angle measurements (Figure S5). Remarkably, all three SAM films exhibited substantially enhanced hydrophobicity compared to PEDOT:PSS, showcasing water contact angles surpassing 50°, which is beneficial for resisting water vapor adsorption.

Device performances and mechanism analysis

To evaluate the potential of three SAMs as HILs for QLEDs, we first fabricated red-emitting QLEDs with the architecture of ITO/PEDOT:PSS or SAMs/(poly(9,9-dioctylfluorene-*alt*-*N*-(4-(*sec*-butylphenyl)-diphenylamine) (TFB)/CdZnSe/ZnS quantum dots/ZnMgO/Al, where TFB served as HTL and ZnMgO as the ETL. The best-performing QLEDs were fabricated by spin coating a 0.5 mg/mL SAM solution in DMSO at 4000 rpm for 40 s, which is a rapid and scalable fabrication process conducive to large-scale production. For comparison study, the devices incorporating PEDOT:PSS and unoptimized Cz as HILs were designated as reference devices.

The normalized EL spectra of four devices as presented in Figure 2A were recorded at a bias voltage of 2 V. All devices display a consistent EL peak at 628 nm, accompanied by a narrow full width at half maximum (FWHM) less than 23 nm (refer to Table 1), reflecting excellent spectral purity. The corresponding Commission Internationale de l'Éclairage (CIE) color coordinates are determined to be (0.68, 0.31). The corresponding current-voltage-luminance (*J-V-L*) characteristics are shown in Figure 2B. Notably, the BCB-Br or BCB HILs based QLEDs present substantially higher current densities than

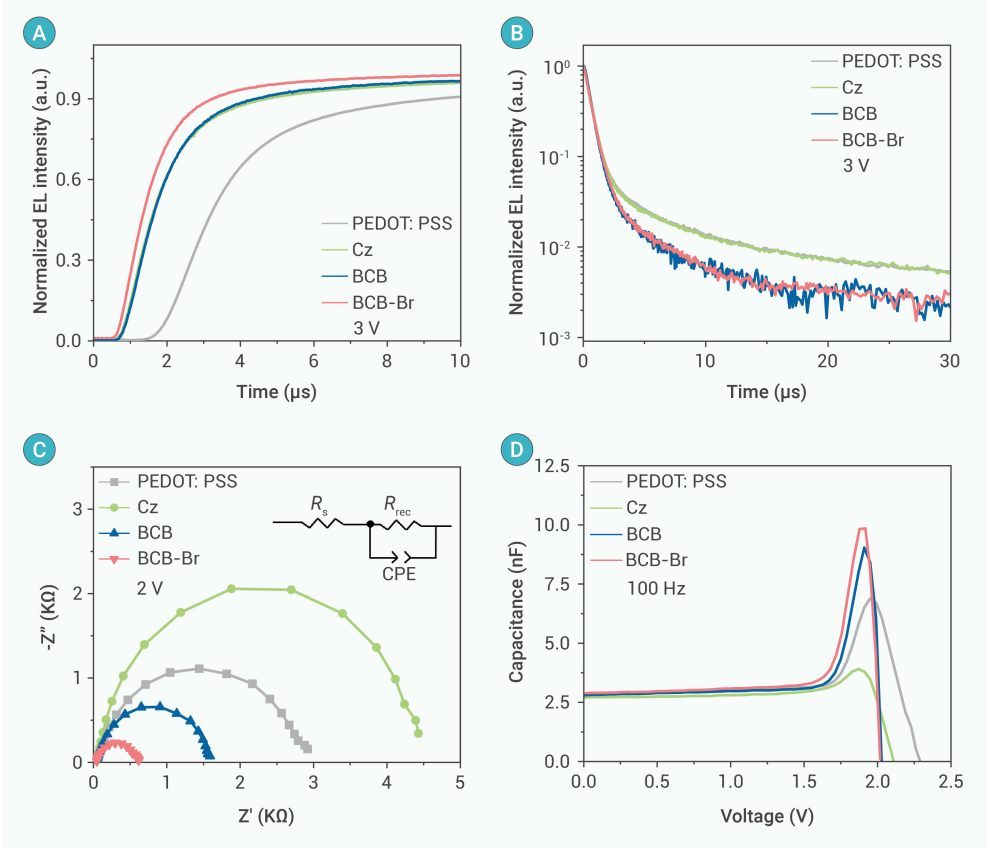

Figure 3. Study on carrier and exciton dynamics of the red-emitting QLEDs utilizing SAMs or PEDOT:PSS as the HILs (A) The rising part of TREL, (B) the decayed part of TREL, (C) the Nyquist plots and (D) the *C-V* characteristics of the devices.

PEDOT:PSS and Cz based counterparts. Among them, the BCB-Br-based device exhibited the highest current density, whereas the Cz-based one demonstrated the lowest. Furthermore, the BCB and BCB-Br devices demonstrated the exceptionally low V_ts of 1.75 and 1.73 V (at a luminance of 1 cd/cm^2), respectively. In contrast, the V_t of the devices based on PEDOT:PSS or Cz exceeded 1.8 V under the same conditions. These findings, in conjunction with the UPS results, suggest that the superior interface modification abilities of BCB and BCB-Br on ITO effectively reduce the hole injection barrier between ITO and TFB, thereby enhancing hole injection efficiency.

Leveraging their remarkable interface modification properties, the SAMs-based QLEDs showcase markedly superior performance metrics relative to the PEDOT:PSS reference devices (Figures 2C-E). The red-emitting device utilizing PEDOT:PSS achieved only a moderate power efficiency (PE) of 41.1 lm/W, a current efficiency (CE) of 27.5 cd/A, and an EQE of 21.6%, which align closely with literature values.[35] In stark contrast, the molecular engineered BCB based devices displayed significantly improved performance parameters with a PE of 44.3 lm/W, a CE of 28.5 cd/A, and an EQE of 21.9%. The optimal BCB-Br HIL endows the red QLEDs with even better luminescence performance, i.e., a PE of 47.0 lm/W, a CE of 30.4 cd/A, and an EQE of 23.3%. A comprehensive EL performance comparison with reported high-efficient CdZnSe/ZnS QDs red QLEDs is plotted in Figure 2F, with detailed data summarized in Table S2. Notably, our BCB-Br HIL based devices achieved the highest and most balanced EL metrics. Considering the subpar EL performance for Cz based device, one can explain with the carbazole's inadequate interfacial modification and suboptimal optoelectronic properties, highlighting the significance of our molecular engineering employed for BCB-Br in optimizing device performance. High reproducibility is also demonstrated for the fabricating QLEDs with solution-processed SAMs HILs (Figure S6).

To elucidate the role of SAMs in regulating charge carrier and exciton dynamics, we performed time-resolved electroluminescence (TREL) measurements on various devices. Upon applying a pulsed voltage, holes are injected sequentially into HIL, HTL and EML at varying intervals, governed by distinct charge mobilities and injection barriers of each layer. Figure 3A presents the initial rise of the TREL curves for each device under a pulse voltage of 3 V. Notably, the delay times (t_d) of the EL intensity curves for three SAMs-based devices are significantly shorter than that of PEDOT:PSS based one. The BCB-Br-based QLEDs demonstrate the shortest t_d of 0.62 μs. The TREL decay curves were further analyzed using a bi-exponential fitting function to determine the exciton lifetimes (Figure 3B). The exciton lifetimes for the BCB-Br and BCB and devices are found to be 2.25 μs and 2.27 μs, respectively, both of which are significantly shorter than those of PEDOT:PSS (3.45 μs) and Cz-based (3.46 μs) devices. These results suggest that BCB-Br HIL effectively promotes hole injection and transport, enabling faster radiative recombination within EML and mitigating non-radiative recombination processes that are typically associated with charge accumulation.[36]

In addition to the exceptional conductivity of SAMs HILs, the reduced interface contact resistance may also contribute to the enhanced hole injection. To validate this hypothesis, we conducted electrochemical impedance spectroscopy (EIS) measurements. The equivalent circuit model composed of series resistance (R_s), recombination resistance (R_{rec}) and constant phase element (CPE) is depicted in Figure 3C,[37,38] with detailed fitting parameters listed in Table S3. The device utilizing PEDOT:PSS exhibited an R_s of 52.79 Ω/cm^2, while for SAMs, the attained R_s value decreased from 55.24 Ω/cm^2 for Cz to 51.52 and 46.45 Ω/cm^2 for BCB and BCB-Br counterparts, respectively. This decline in R_s correlates with the easier hole injection, resulting in the lower V_t for devices based on BCB and BCB-Br HILs. Regarding R_{rec}, the BCB-Br-based device showcased the lowest fitted value of 558 Ω/cm^2, markedly lower than 2801 Ω/cm^2 recorded for PEDOT:PSS-based one. Furthermore, the CPE value for the device utilizing BCB-Br (12.6×10^{-9} S Sec^n/cm^2) was slightly higher than those with BCB (8.5×10^{-9} S Sec^n/cm^2) and PEDOT:PSS (9.1×10^{-9} S Sec^n/cm^2) HILs. These disparities indicate a more efficient exciton recombination within EML for devices incorporating BCB-Br,[39] well explaining the reduced exciton lifetimes observed in the TREL measurements. Collectively, these findings imply that the presence of BCB-Br not only mitigates interface contact resistance but promotes more efficient exciton formation and recombination between HTL and ITO.

In parallel, capacitance-voltage (*C-V*) measurements were conducted at a fixed frequency of 100 Hz (Figure 3D). The geometric capacitance of all devices was maintained at approximately 2.5 nF, reflecting consistent structural integrity and comparable dielectric properties across the samples.[40] The PEDOT:PSS-based device exhibited a moderate capacitance peak of 6.9 nF. In contrast, the CZ-based device displayed a maximum capacitance peak of 3.9 nF, while the capacitance peaks for BCB and BCB-Br-based devices were notably enhanced to 9.0 nF and 9.8 nF, respectively. This increase in capacitance suggests that a much greater number of charge carriers can be injected into BCB-Br-based device. Following the capacitance peak, a sharper decline is observed in both devices utilizing BCB and BCB-Br, indicative of rapid electron-hole recombination within these devices.[38,41] Furthermore, the lower capacitance peak voltages for BCB-Br and BCB devices imply a much reduced built-in potential, which may contribute to the lower V_t in these devices.[38,42] Collectively, the optimal BCB-Br demonstrates efficient charge injection, rapid recombination, and improved exciton dynamics. The synergistic effects of these merits significantly enhance device performance, highlighting the reliability of our comprehensive SAM molecular design strategy.

The versatility of HILs across different spectral systems is paramount for their scalable application. Consequently, we selected BCB-Br as the repre-

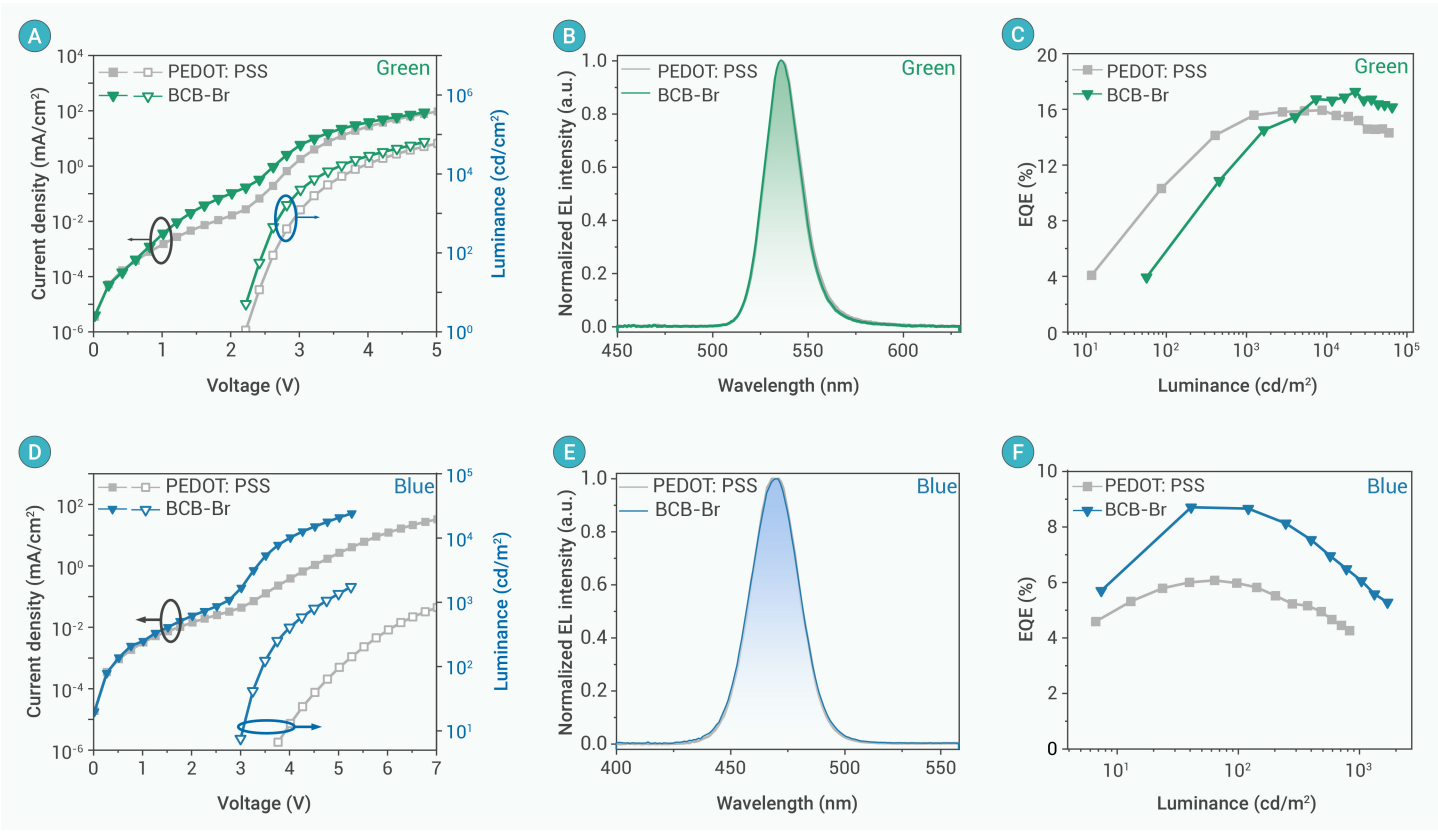

Figure 4. The device performance of representative green and blue-emitting QLEDs utilizing BCB-Br or PEDOT:PSS HILs (A) *J-V-L* curves, (B) Normalized EL spectra, and (C) EQE curves of green-emitting QLEDs. (D) *J-V-L*, (E) Normalized EL spectra, and (F) EQE curves of blue-emitting QLEDs.

Table 2. EL performance parameters of BCB-Br or PEDOT:PSS-based green and blue QLEDs

Devices	HILs	V_t[a] (V)	EQE[b] (%)	λ_{EL}[c] (nm)	FWHM[d] (nm)	CIE[e] (x, y)
Green	PEDOT:PSS	2.40	15.9	536	21.9	(0.23, 0.73)
	BCB-Br	2.27	17.3	536	21.6	(0.23, 0.73)
Blue	PEDOT:PSS	3.86	6.1	471	24.3	(0.13, 0.07)
	BCB-Br	3.06	8.7	471	24.9	(0.13, 0.07)

[a] Turn-on voltage at a luminance of 10 cd/m^2. [b] Maximum external quantum efficiency. [c] Peak wavelength of the EL spectrum. [d] Full-width at half-maximum of the EL spectrum. [e] Commission International de l'Eclairage 1931 color coordinates.

sentative SAMs to evaluate its performance in green and blue QLEDs. The EL performance curves for the corresponding green and blue devices are illustrated in Figure 4, with the performance parameters summarized in Table 2. For the green QLEDs, an emission peak at 536 nm is observed, accompanied by a FWHM of approximately 22 nm (refer to Figure 4B). Notably, the BCB-Br based green QLED exhibits a lower V_t (2.27 V) than PEDOT:PSS counterpart (2.40 V), attributable to the reduced hole injection barrier (Figure 4A). This improvement culminates in a remarkable EQE of 17.3% for BCB-Br-based device, significantly surpassing that of PEDOT:PSS based one (Figure 4C). A more pronounced trends are observed in the blue-emitting QLEDs, where the V_t of BCB-Br based device is reduced by 0.8 V relative to its PEDOT:PSS-based analog, leading to an enhancement of over 40% in EQE for the blue QLEDs (Figures 4D–F). These results underscore the distinctive advantages of BCB-Br as a versatile high-efficient HILs for all RGB QLEDs.

CONCLUSION

In summary, we have for the first time reported the conjugation-terminal engineered SAMs as versatile HILs for full-color QLEDs. These materials can rapidly anchor to ITO surface and form high-quality monolayers with high electrical conductivity. The asymmetric conjugation extension and bromination engineering on carbazole core of SAMs significantly enhances their dipole moment and film formation quality. The optimized energy level alignment at HIL/HTL interface reduces the contact resistance and thus facilitates hole injection. The optimal BCB-Br SAM endows red QLEDs with a remarkable 23.3% EQE and a reduced V_t of 1.73 V, outperforming conventional PEDOT:PSS and carbazole SAMs-based counterparts. Moreover, BCB-Br HIL readily endows red QLEDs with high and balanced PE/CE values, demonstrating exceptional versatility in both green and blue QLEDs. This study not only presents an optimal HIL choice for various QLEDs but elucidates the impact of molecular engineering of SAMs on device performance.

REFERENCES

1. Won Y.-H., Cho O., Kim T. et al. (2019). Highly efficient and stable InP/ZnSe/ZnS quantum dot light-emitting diodes. *Nature* **575**:634–638. DOI:10.1038/s41586-019-1771-5
2. Yoo J., Lee K., Yang U. J. et al. (2024). Highly efficient printed quantum dot light-emitting diodes through ultrahigh-definition double-layer transfer printing. *Nat. Photonics* **18**:1105–1112. DOI:10.1038/s41566-024-01496-x
3. Jang E. and Jang H. (2023). Review: Quantum dot light-emitting diodes. *Chem. Rev.* **123**:4663–4692. DOI:10.1021/acs.chemrev.2c00695
4. Lei S., Xiao Y., Yu K. et al. (2023). Revisiting hole injection in quantum dot light-emitting diodes. *Adv. Funct. Mater.* **33**:2305732. DOI:10.1002/adfm.202305732
5. Shen, H., Gao, Q., Zhang, Y. et al. (2019). Visible quantum dot light-emitting diodes

with simultaneous high brightness and efficiency. *Nat. Photonics* **13**:192–197. DOI:10.1038/s41566-019-0364-z
6. Xu H., Song J., Zhou P. et al. (2024). Dipole-dipole-interaction-assisted self-assembly of quantum dots for highly efficient light-emitting diodes. *Nat. Photonics* **18**:186–191. DOI:10.1038/s41566-023-01344-4
7. Kim T., Kim K.-H., Kim S. et al. (2020). Efficient and stable blue quantum dot light-emitting diode. *Nature* **586**:385–389. DOI:10.1038/s41586-020-2791-x
8. Peng J., Wang T., Wang R. et al. (2024). Efficient perovskite light-emitting diodes achieved by suppressing the acidic surface of PEDOT:PSS films. *Chem. Eng. J* **485**:149668. DOI:10.1016/j.cej.2024.149668
9. Zhao J., Chen F., Jia H. et al. (2023). Boosting Cu-In-Zn-S-based quantum-dot light-emitting diodes enabled by engineering Cu-NiOx/PEDOT:PSS bilayered hole-Injection layer. *Small* **20**:2307115. DOI:10.1002/smll.202307115
10. Zhang Y., Zhan Y., Yuan G. et al. (2024). Record high external quantum efficiency of 20% achieved in fully solution-processed quantum dot light-emitting diodes based on hole-conductive metal oxides. *J. Colloid Interface Sci.* **660**:746–755. DOI:10.1016/j.jcis.2024.01.099
11. Lin J., Dai X., Liang X. et al. (2019). High-performance quantum-dot light-emitting diodes using NiOx hole-injection layers with a high and stable work function. *Adv. Funct. Mater.* **30**:1907265. DOI:10.1002/adfm.201907265
12. Zhuo M.-P., Liang F., Shi Y.-L. et al. (2017). WO_3 nanobelt doped PEDOT:PSS layers for efficient hole-injection in quantum dot light-emitting diodes. *J. Mater. Chem. C* **5**:12343–12348. DOI:10.1039/c7tc04575a
13. Yu H., Liu Z., Ren Z. et al. (2024). Improved molecular packing of self-assembled monolayer charge injectors for perovskite light-emitting diodes. *J. Phys. Chem. Lett.* **15**:6705–6711. DOI:10.1021/acs.jpclett.4c01264
14. Li N., Xia Y., Lou Y. H. et al. (2024). Dual-functional self-assembled molecule enabling high-performance deep-blue perovskite light-emitting diodes. *Adv. Funct. Mater.* **34**:2411227. DOI:10.1002/adfm.202411227
15. Li M., Liu M., Qi F. et al. (2024). Self-assembled monolayers for interfacial engineering in solution-processed thin-film electronic devices: design, fabrication, and applications. *Chem. Rev.* **124**:2138–2204. DOI:10.1021/acs.chemrev.3c00396
16. Li C., Chen Y., Zhang Z. et al. (2024). Pros and cons of hole-selective self-assembled monolayers in inverted PSCs and TSCs: extensive case studies and data analysis. *Energy Environ. Sci.* **17**:6157–6203. DOI:10.1039/d4ee02492c
17. Aktas E., Phung N., Köbler H. et al. (2021). Understanding the perovskite/self-assembled selective contact interface for ultra-stable and highly efficient p–i–n perovskite solar cells. *Energy Environ. Sci.* **14**:3976–3985. DOI:10.1039/d0ee03807e
18. Gedda M., Gkeka D., Nugraha M.I. et al. (2022). High-efficiency perovskite-organic blend light-emitting diodes featuring self-assembled monolayers as hole-injecting interlayers. *Adv. Energy Mater.* **13**:2201396. DOI:10.1002/aenm.202201396
19. Xu S.H., Xu J.Z., Tang Y.B. et al. (2024). Interfacial dipole engineering for energy level alignment in NiOx-based quantum dot light-emitting diodes. *Small* **20**:2411227. DOI:10.1002/smll.202403325
20. Tan Q., Li Z., Luo G. et al. (2023). Inverted perovskite solar cells using dimethylacridine-based dopants. *Nature* **620**:545–551. DOI:10.1038/s41586-023-06207-0
21. Zhao K., Liu Q., Yao L. et al. (2024). *peri*-Fused polyaromatic molecular contacts for perovskite solar cells. *Nature* **632**:301–306. DOI:10.1038/s41586-024-07712-6
22. Jiang, Y. Oh N. and Shim M. (2016). Double-heterojunction nanorod light-emitting diodes with high efficiencies at high brightness using self-assembled monolayers. *ACS Photonics* **3**:1862–1868. DOI:10.1021/acsphotonics.6b00371
23. Lin J.-Y., Hsu F.-C., Chao Y.-C. et al. (2023). Self-assembled monolayer for low-power-consumption, long-term-stability, and high-efficiency quantum dot light-emitting diodes. *ACS Appl. Mater. Interfaces* **15**:25744–25751. DOI:10.1021/acsami.3c01566
24. Ali F., Roldán - Carmona C., Sohail M. et al. (2020). Applications of self-assembled monolayers for perovskite solar cells interface engineering to address efficiency and stability. *Adv. Energy Mater.* **10**:2002989. DOI:10.1002/aenm.202002989
25. Li E., Liu C., Lin H. et al. (2021). Bonding strength regulates anchoring-based self-assembly monolayers for efficient and stable perovskite solar cells. *Adv. Funct. Mater.* **31**:2103847. DOI:10.1002/adfm.202103847
26. Al-Ashouri A., Köhnen E., Li B. et al. (2020). Monolithic perovskite/silicon tandem solar cell with >29% efficiency by enhanced hole extraction. *Science* **370**:1300–1309. DOI:10.1126/science.abd4016
27. Kim S.Y., Cho S.J., Byeon S.E. et al. (2020). Self-assembled monolayers as interface engineering nanomaterials in perovskite solar cells. *Adv. Energy Mater.* **10**:2002606. DOI:10.1002/aenm.202002606
28. Magomedov A., Al-Ashouri A., Kasparavičius E. et al. (2018). Self-assembled hole transporting monolayer for highly efficient perovskite solar cells. *Adv. Energy Mater.* **8**:1801892. DOI:10.1002/aenm.201801892
29. He R., Wang W., Yi Z. et al. (2023). All-perovskite tandem 1-cm^2 cells with improved interface quality. *Nature* **618**:80–86. DOI:10.1038/s41586-023-05992-y
30. Wang W., Wei K., Yang L. et al. (2023). Dynamic self-assembly of small molecules enables the spontaneous fabrication of hole conductors at perovskite/electrode interfaces for over 22% stable inverted perovskite solar cells. *Mater. Horiz.* **10**:2609–2617. DOI:10.1039/d3mh00219e
31. Wang W., Liu X., Wang J. et al. (2023). Versatile self-assembled molecule enables high-efficiency wide-bandgap perovskite solar cells and organic solar cells. *Adv. Energy Mater.* **13**:2300694. DOI:10.1002/aenm.202300694
32. Duan J., Wang M., Wang Y. et al. (2021). Effect of side-group-regulated dipolar passivating molecules on $CsPbBr_3$ perovskite solar cells. *ACS Energy Lett.* **6**:2336–2342. DOI:10.1021/acsenergylett.1c01060
33. Kim T.H., Kim B.W. and Im S.H. (2024). A self-assembling molecule for improving the mobility in PEDOT:PSS hole transport layer for efficient perovskite light-emitting diodes. *Adv. Electron. Mater.* **11**:2400626. DOI:10.1002/aelm.202400626
34. Hotchkiss P. J., Jones S. C., Paniagua S. A. et al. (2012). The modification of indium tin oxide with phosphonic acids: mechanism of binding, tuning of surface properties, and potential for use in organic electronic applications. *Acc. Chem. Res.* **45**:337–346. DOI:10.1021/ar200119g
35. Chen Q., Hu Y., Lin J. et al. (2024). Phenethylammonium bromide interlayer for high-performance red quantum-dot light emitting diodes. *Nanoscale Horiz.* **9**:465–471. DOI:10.1039/d3nh00495c
36. Wang F., Zhang H., Lin Q. et al. (2020). Suppressed efficiency roll-off in blue light-emitting diodes by balancing the spatial charge distribution. *J. Mater. Chem. C* **8**:12927–12934. DOI:10.1039/d0tc03295f
37. Liu Y., Liu Q., Ding L. et al. (2024). Enhancing the efficiency and stability of inverted perovskite solar cells and modules through top interface modification with N-type semiconductors. *Angew. Chem. Int. Ed.* **64**:e202416390. DOI:10.1002/anie.202416390
38. Qu X. and Sun X. (2023). Impedance spectroscopy for quantum dot light-emitting diodes. *J. Semicond.* **44**:091603. DOI:10.1088/1674-4926/44/9/091603
39. Wang J., Li M., Cai B. et al. (2024). Matched electron-transport materials enabling efficient and stable perovskite quantum-dot-based light-emitting diodes. *Angew. Chem. Int. Ed.* **63**:e202410689. DOI:10.1002/anie.202410689
40. Ma Z., Sun Z., Yang H. et al. (2023). Interface-mediation-enabled high-performance near-infrared AgAuSe quantum dot light-emitting diodes. *J. Am. Chem. Soc.* **145**:24972–24980. DOI:10.1021/jacs.3c10214
41. Qu X., Ma J., Wang K. et al. (2024). Characteristic voltages and times from capacitance–voltage analysis of quantum dot light-emitting diodes. *Appl. Phys. Lett.* **124**:263503. DOI:10.1063/5.0221019
42. Wang R., Xiang H.Y., Zhang C. et al. (2024). A record-breaking low turn-on voltage blue QLED via reducing built-in potential. *Nano Res.* **17**:10446–10452. DOI:10.1007/s12274-024-6570-0

FUNDING AND ACKNOWLEDGMENTS

This work was financially supported by National Natural Science Foundation of China (Nos. 22375170, 61975256, and 52373195), Shenzhen Science and Technology Program (JCYJ20230807091313027), Fostering Talents Projects of Innovation Laboratory for Sciences and Technologies of Energy Materials of Fujian Province (IKKEM) (HRTP-[2022]-45), Nanqiang Outstanding Professors Program of Xiamen University, Outstanding post-doctoral support project of Fujian Province and the Plans for the Recruitment of Top-notch Talent by Fujian Province and Xiamen. G. X. acknowledged the funding support from the Key Science and Technology Project on Future Industry of Xiamen City (No. 3502Z20231052). J. L. and J. H. acknowledged the financial support from the Perovskite Thin-Film Innovation Technology Centre（No: YZCXPT2022104） and the Natural Science Foundation of Jiangsu Province (No. BK20231222). The authors thank the Tan Kah Kee Innovation Laboratory (IKKEM) of Xiamen University for the assistance on measurements. Mesolight (Suzhou) is gratefully acknowledged for providing red, green and blue CdZnSe/ZnS QDs and ZnMgO solutions. The funders had no role in study design, data collection and analysis, decision to publish, or preparation of the manuscript.

AUTHOR CONTRIBUTIONS

Tang, W. and Xie, G. conceived and designed the research. Wang, W. designed and synthesized the SAMs and provided the relevant theoretical calculations. Chen, Q. fabricated the devices and conducted the characterizations. Hua, G., Lin, J. and Huang, J. assisted in device characterizations and data analysis. Wang, W. and Tang, W. wrote the initial draft and all authors contributed to the final manuscript.

DECLARATION OF INTERESTS

The authors declare no competing interests.

DATA AND CODE AVAILABILITY

Data are available from the corresponding author upon reasonable request.

SUPPLEMENTAL INFORMATION

It can be found online at https://doi.org/10.59717/j.xinn-mater.2025.100151